



Dislocation loop bias and void swelling in irradiated α -iron from mesoscale and atomistic simulations

Ziang Yu¹ & Haixuan Xu¹  

Dislocation loops are ubiquitous in irradiated materials, and dislocation loop bias plays a critical role in void swelling. However, due to complicated interactions between dislocation loops and point defects, it is challenging to evaluate the bias factors of dislocation loops. Here, we determine the bias of sessile $\langle 100 \rangle$ loops in α -iron using a recently developed atomistic approach based on the lifetime of point defects. We establish a mechanistic understanding of the loop interaction based on the diffusion tendency of point defects near the loop core region. Mobile self-interstitial atoms tend to be absorbed from the edge of the loop, and a trapping region perpendicular to the habit plane of the loop exists. The dislocation loop bias is found to be substantially lower than those of straight dislocations in α -iron and should be included in swelling rate estimates. With the obtained sink strength and bias values, agreement is achieved with experimental results for both absolute values and temperature dependence.

¹Department of Materials Science and Engineering, The University of Tennessee, Knoxville, TN 37996, US. ✉email: xhx@utk.edu

The unit interactions of defects at atomistic scales during irradiation processes^{1–4} could significantly affect macroscopic material properties, such as void swelling^{5–11}, degrading mechanical performance, and limiting the lifetime of structural components in fission and fusion reactors^{12,13}. The generally accepted mechanism for void swelling is the preferential absorption of mobile interstitials over vacancies at certain sinks, defined as bias^{12,14,15}. The bias factor values for different types of sinks are essential parameters for modeling void swelling and overall microstructural evolution. However, it is fundamentally challenging to study the underlying complex defect interaction processes between sinks and point defects, which are too fast to observe using experimental tools like transmission electron microscopy (TEM) and too slow to model by conventional atomistic simulations^{16–20}. Moreover, some previous theoretical models, e.g., in α -iron, have overestimated bias values by an order of magnitude compared with those estimated from experimental results^{10,21,22}. Therefore, to precisely evaluate the bias in structural materials, a fundamental understanding of interactions between sinks and radiation-induced defects is essential.

One of the dominant microstructural features of sinks for mobile point defects in irradiated materials is dislocation. Dislocation bias factors have been widely studied using elasticity theory^{9,10}, production bias model^{23,24}, dipole tensor method^{22,25}, and numerical approaches^{26–29}. However, it is still challenging to achieve close agreement with experimental results of swelling rates based only on dislocation bias.

Dislocation loops are also ubiquitous in irradiated α -iron^{30–38} and are known as biased sinks for mobile point defects³⁹, including interstitials and vacancies. Comparatively, dislocation loop bias is much less frequently studied due to the extremely complex three-dimensional strain field near it^{40,41}. For instance, the formalism of the strain field around a dislocation loop is daunting even in an infinite isotropic material^{42,43}, and it is challenging to apply these complex strain field equations in the bias calculations. Therefore, different approximations were made

in previous theoretical efforts. Brailsford et al.^{15,44} originally developed a rate-theory framework for describing void swelling and assessed the role of dislocation loop bias. This model was employed by Bullough and Woo et al.^{39,41} to calculate sink strength and bias factors of dislocation loops with the effective medium approximation. In these studies, the dislocation loop is considered a spherical sink. Dubinko et al.⁴⁵ employed a toroidal internal boundary condition for dislocation loops, which emphasized the importance of sink topology. The description of dislocation loop topology was improved by Rouchette et al.^{40,46} through the phase-field method⁴⁷, which determined sink strength more accurately by considering the anisotropic elastic interactions between point defects and loops. Nevertheless, there have been two significant limitations. First, the effects of the core region near the dislocation loop cannot be accurately modeled because the atomistic details of loops were not considered. Second, the influences of dislocation loops on defect transport properties, e.g., migration energy barriers (MEBs), are inaccurate since the interactions between point defects and dislocation loops are stronger than those between point defects and straight dislocations, due to the larger strain field exhibited by the loops⁴⁶. This will result in regions where the actual saddle points differ noticeably from the estimations based on the isotropic/anisotropic elasticity theory approaches, subsequently impacting calculations of capture efficiencies, sink strengths, and loop bias.

In this study, the dislocation loop bias is calculated based on the lifetime of point defects. Dislocation loops with radii from 1 nm to 5 nm are studied based on the experimentally reported loop sizes in neutron-irradiated iron³¹. Only sessile $\langle 100 \rangle$ loops are considered since they are the dominant type in bcc iron when the temperature is higher than 548 K^{31,48,49}. Spontaneous absorption region (SAR) is calculated based on the binding energy using Large-scale Atomic/Molecular Massively Parallel Simulator (LAMMPS)⁵⁰, in which the mobile point defects are considered absorbed by the loop. The MEBs of point defects at every lattice point near the dislocation loop are calculated using

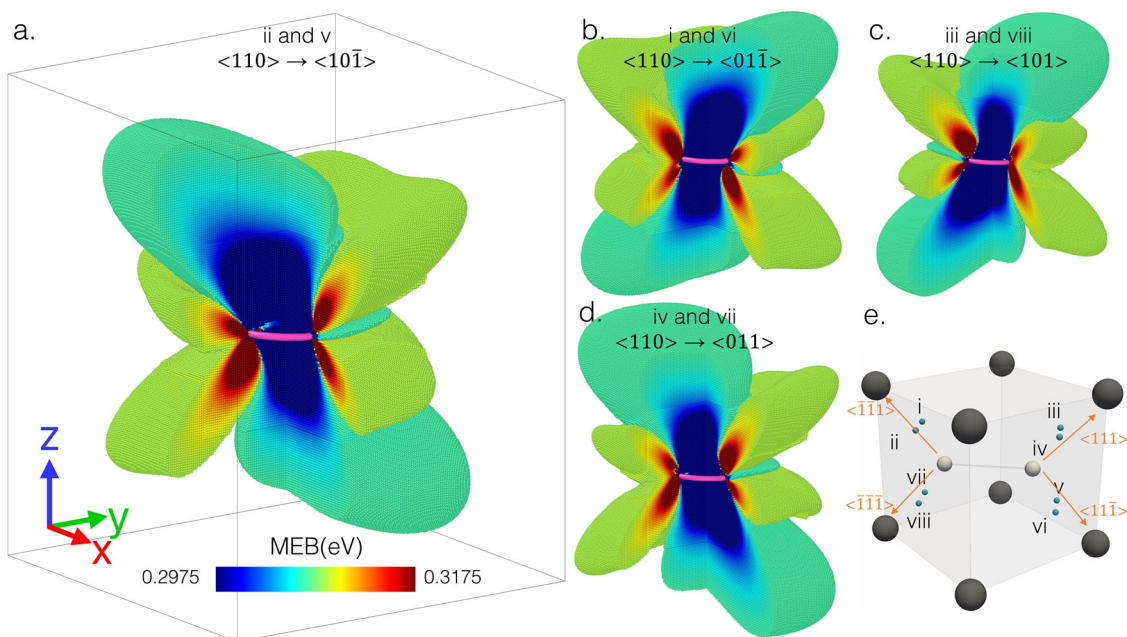


Fig. 1 Migration energy barriers of the [110] dumbbell saddle points in bcc iron. **a–d** Each contain the MEB map of two saddle points given by blue spheres in **(e)**. Figure **(a)** for the saddle point ii and v, **(b)** for i and vi, **(c)** for iii and viii, and **(d)** for iv and vii. Axes x, y, and z in **(a)** stand for $\langle 100 \rangle$, $\langle 010 \rangle$, and $\langle 001 \rangle$ directions. White spheres in **(e)** represent the [110] dumbbell. MEBs close to bulk values (± 0.001 eV) are intentionally hidden. The dislocation loop calculated by dislocation analysis (DXA) by Ovito⁷¹ is shown in pink. Note that the MEBs of saddle points (ii and v, i and vi, iii and viii, iv and vii in Fig. 1e) look identical, although there exists a very small numerical difference.

the self-evolving atomistic kinetic Monte Carlo (SEAKMC) package^{51–53}. The statistical diffusion tendency considering all different dumbbell configurations is analyzed at each atomic position close to the loop. The point defect lifetime is then calculated using atomistic kinetic Monte Carlo (AKMC), with which the capture efficiency, sink strength, dislocation loop bias, and swelling rates are also calculated. Temperature, loop size, and loop density effects are systematically studied. The obtained bias factors are compared with previous theoretical results of loop bias and straight dislocation bias. Estimated swelling rates and experimental data are also compared, and the effects of various factors that influence void swelling in irradiated α -iron are discussed.

Results and discussion

Migration energy barriers (MEBs). Figure 1 shows the MEBs calculated based on obtained saddle point configurations (illustrated in Fig. 1e with blue spheres labeled from i to viii, respectively) associated with the first nearest neighbor diffusion of the [110] dumbbell. For instance, the MEBs toward $[\bar{1}\bar{1}1]$ direction through saddle point ii are given in Fig. 1a. It is found that MEBs are highly anisotropic and exhibit a complex dependency on the position relative to the dislocation loop due to the previously mentioned complicated strain field of the dislocation loop. For the [110] dumbbell, the region with lower MEBs is primarily along the normal direction of the loop habit plane, and the region with higher MEBs circles the loop. In addition to the change in energy barriers, note that dumbbell diffusion via a given saddle point leads to a different final configuration from the initial configuration. Taking a [110] dumbbell as an example, the final configuration will turn into a $[10\bar{1}]$ dumbbell through saddle point ii or v. Besides the [110] dumbbell, all five other dumbbell configurations present distinct MEB dependencies, which have been shown in Supplementary Fig. 1 together with the corresponding final configurations through different saddle points. Since the strain field is not homogeneous and since previous researchers^{39,45} also stated that the loop bias was found to depend on the loop nature and the point defect shape at the saddle point, the spatial dependence of MEBs in the vicinity of the dislocation loop is thus fully considered, which is challenging using the conventional rate theory approaches.

We find the cumulative effects of MEBs and the configurations of dumbbells contribute significantly to the bias factor. We conduct comparative simulations to demonstrate these effects (see data in Table 1, which shows the bias factor (0.0089) of a 5 nm loop at 573 K at a dislocation loop density equal to 10^9 cm^{-2}). For comparison, a significant overestimation (6.8 times higher) is observed if the MEBs calculated using SEAKMC are replaced by those calculated using only the dipole tensor method. Correspondingly, we notice an obvious underestimation of capture efficiencies for both self-interstitial atoms (SIAs) and vacancies using the elasticity method. This

significant difference is caused by the cumulative effect of the huge number of MEBs and the number of diffusive steps of each trajectory (e.g., about 0.7 million diffusive steps when the dislocation loop density equals $7 \times 10^9 \text{ cm}^{-2}$ at 573 K), although the differences in MEBs at most of the atomic positions are small (details in Supplementary Fig. 2). We further show the effect of dumbbell configurations by considering only one of the six dumbbell configurations in the model. We find two different bias factors for different dumbbell configurations due to crystallographic symmetry. Using either [110] or $[\bar{1}\bar{1}0]$ configuration leads to a negative bias factor around -0.01 ; [101], $[10\bar{1}]$, $[011]$, and $[01\bar{1}]$ dumbbells result in a much higher value, which is about an order of magnitude higher than the value from our model. Thus, it is essential to include all possible initial configurations and the configuration change at each diffusive step in KMC simulations.

Point defect transport mechanism near dislocation loop. Near the dislocation loop core region, SIA diffusion shows two pathways, illustrated in Fig. 2a. In Path I, a mobile SIA near the loop habit plane tends to be absorbed directly by the edge of the loop. In Path II, a SIA far from the loop habit plane migrates toward the habit plane region along the curved arrow paths. This transport behavior in Path II results from a strong repulsive interaction between the loop and the SIA. Comparatively, for vacancy transport, only one path is found, wherein a mobile vacancy tends to be absorbed by the loop from $\sim 35^\circ$ to the habit plane, as shown in Fig. 2b.

This point defect transport mechanism is revealed by analyzing the expected diffusion direction of a point defect at every atomic position, termed as diffusion tendency (details in Supplementary Note 2). Figure 2c shows the diffusion tendency of a SIA surrounding a 2 nm [100] loop, where the SARs are labeled with grey spheres. The (110) plane cross-section is shown since it has the highest atomic density, and the SIAs on this plane primarily show diffusion tendencies parallel to this plane. Four regions with different SIA transport behaviors are observed and labeled by α , β , γ , and δ . Region α is an attractive region (red arrows) indicating that a [100] interstitial loop generally absorbs SIAs from the edge of the loop, which corresponds to Path I. Region γ represents a repulsive region (blue arrows), and SIAs in this region tend to diffuse away from the loop. The fan-shaped region located near region γ is region β . Although the region β is attractive, SIAs in this region are prevented from being absorbed by the loop directly due to the strong repulsion in region γ . This phenomenon leads to the formation of a special region, labeled δ . Since most of the SIAs tend to diffuse towards the center of δ , they can be regarded as being trapped in δ and have a high chance to stay there for extra diffusive steps. This causes an increase in the lifetime of SIAs (τ_i) and lower absorption efficiency of SIAs. The trapping phenomenon in δ , the attractive influence in β , and the repulsive influence in γ lead to curved paths for the diffusion of SIAs, which corresponds to Path II. In comparison, Fig. 2d shows the diffusion tendency of a vacancy, where the attractive interaction between the loop core and vacancies is $\sim 35^\circ$ to the habit plane (red arrows). Vacancies are easily absorbed by the loop center in region γ , while they are repulsed in region β . Recent research by McElfresh et al.^{54,55} using a phase field method has shown a similar behavior of vacancies approaching interstitial loops in Mo, which is that vacancies diffuse toward the loop from compressive stress gradients rather than directly from the habit plane, demonstrating highly anisotropic diffusion of point defects in response to the spatially complex stress fields created by the dislocation loops. The observations

Table 1 Loop bias and capture efficiencies under different simulation conditions.

	Bias	Z_i	Z_v
This Study	0.0089	1.46	1.45
Dipole tensor method	0.0605	1.26	1.19
[110] dumbbell only	-0.0103	1.44	1.45
[101] dumbbell only	0.1302	1.64	1.45

[110] dumbbell and $[\bar{1}\bar{1}0]$ dumbbell have almost the same results, the other four dumbbell configurations have similar results, which are different from those from [110] dumbbell. The temperature is 573 K and the loop density is 10^9 cm^{-2} (equals $3.18 \times 10^{20} \text{ m}^{-3}$ when the loop radius is 5 nm) for all these simulations.

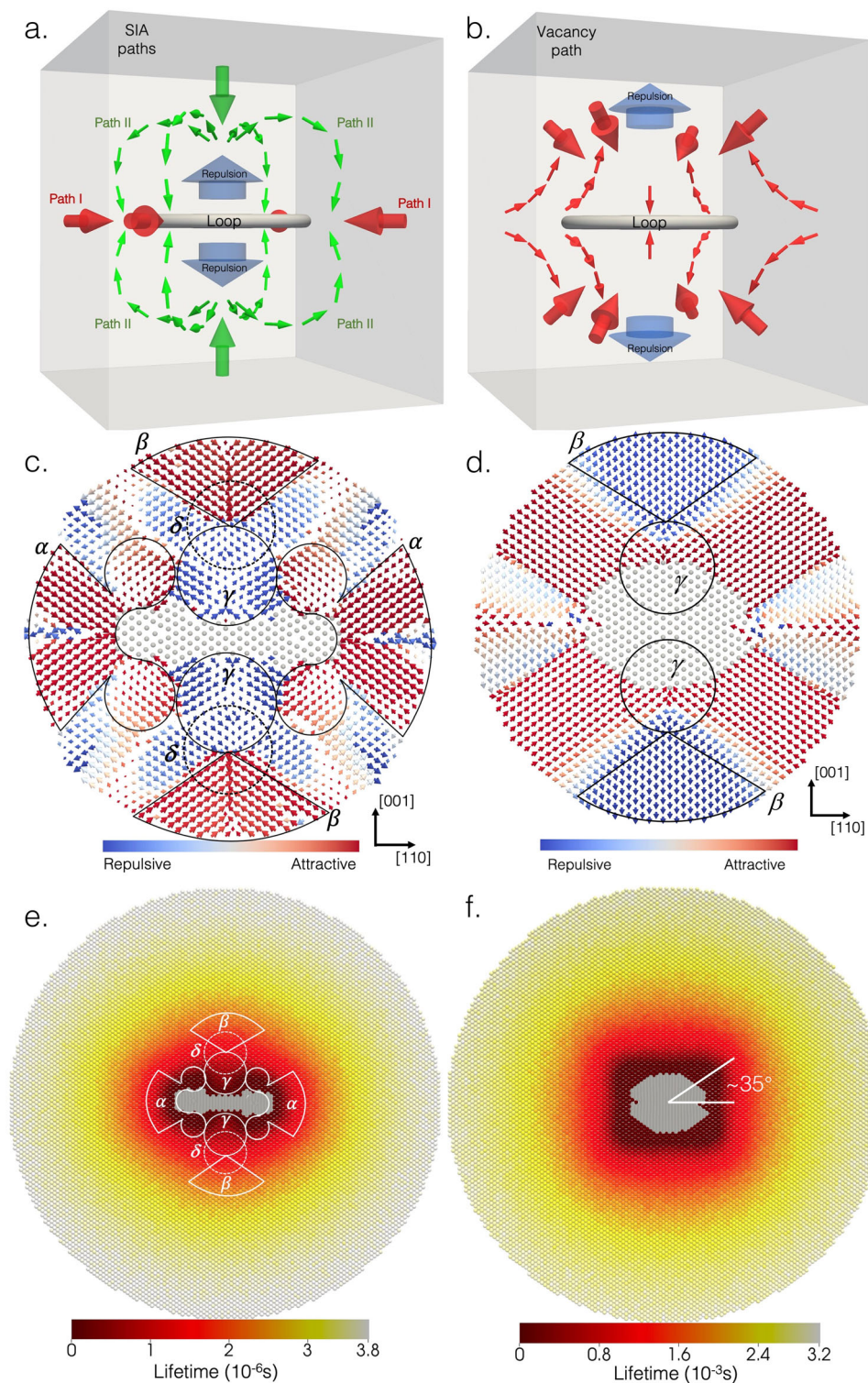


Fig. 2 The point defect transport mechanisms. Diffusion paths of SIAs (a) and vacancies (b) are both provided together with the repulsive regions near the loop. The diffusion tendency of SIAs (c) and vacancies (d) are calculated at each atomic position. The lifetime of SIAs (e) and vacancies (f) are calculated at 573 K and the loop density is $2.24 \times 10^{10} \text{ cm}^{-2}$ (equals $1.78 \times 10^{22} \text{ m}^{-3}$ when the loop radius is 2 nm). The SARs are labeled in grey atoms in the center of the simulation system for (c–f).

of point defect – loop interactions are commensurate with the calculated stress/strain field of the loop (details in Supplementary Fig. 3).

This mechanism is also supported by the lifetime of SIAs (Fig. 2e) and vacancies (Fig. 2f) around the loop. In Fig. 2e, the lifetime of a SIA in α is comparatively shorter than that of other regions with a

similar distance to the loop surface. For a SIA in γ , the lifetime pattern indicates the diffusion trajectories are much longer than those being directly absorbed by the loop, despite the proximity of region γ to the loop center. In Fig. 2f, the lifetime of vacancies at $\sim 35^\circ$ to the habit plane is much shorter than those along other directions, which agrees with the diffusion tendency analysis.

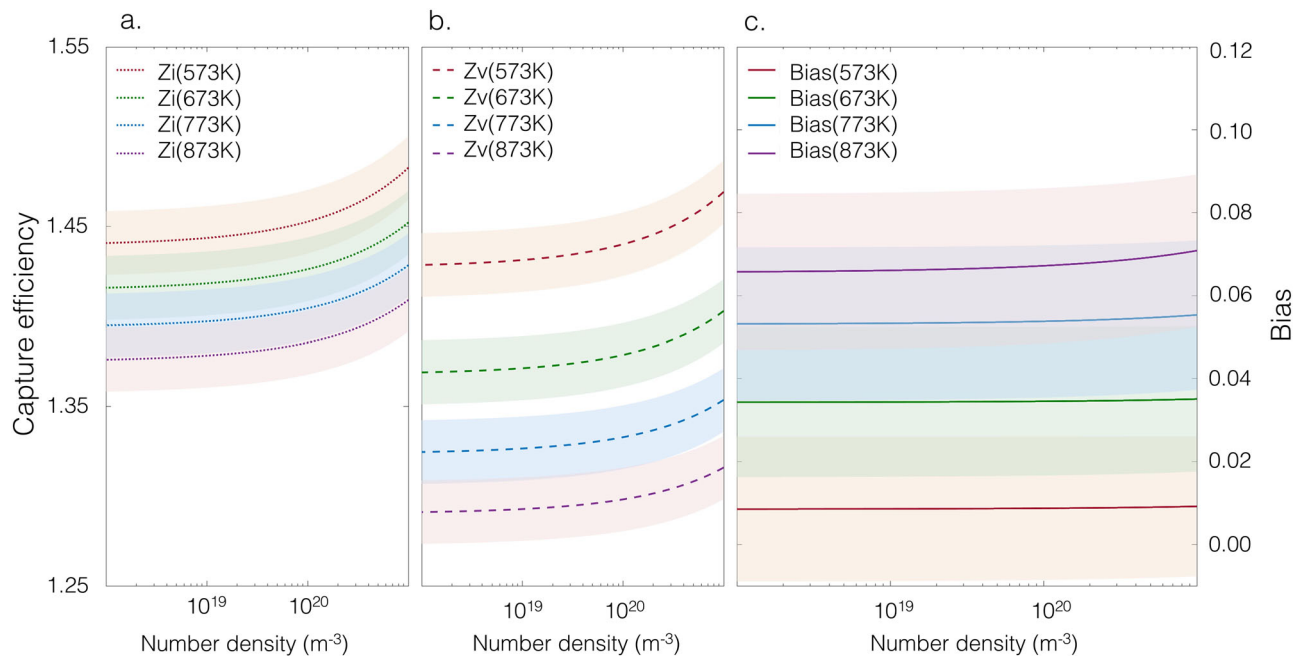


Fig. 3 Calculated capture efficiency and bias as a function of the loop density. **a** Capture efficiencies of interstitials. **b** Capture efficiencies of vacancies. **c** Bias factors of a 5 nm [100] loop.

Capture efficiency and bias of <100> loops. Capture efficiency and bias of loops with radii from 1 nm to 5 nm are calculated with the obtained lifetimes. We find that loops with radii between 2 nm and 5 nm show lower bias factors (≤ 0.02 at 573 K, details in Supplementary Fig. 4) than that of a 1 nm loop (0.17 at 573 K). Since loops with sizes larger than 5 nm are commonly observed in irradiated iron^{31,34,35}, the results of a 5 nm [100] loop as a function of dislocation loop density are shown in Fig. 3 as an example. The capture efficiency of a SIA (Z_i , Fig. 3a), a vacancy (Z_v , Fig. 3b), and the bias factors (Fig. 3c) decrease with decreasing loop density, which is consistent with previous calculations^{39–41,45,46}. At a given temperature and loop density, Z_i is greater than Z_v , due to the respective difference in the interaction energy⁵⁶. The values of both Z_v and Z_i decrease with increasing temperature from 573 K to 873 K; however, the bias factors increase with rising temperatures. This trend differs from the calculation of vacancy loop bias by Woo et al.³⁹ and dislocation bias by Chang et al.^{26,27}, Bakaev et al.²⁸, and Seif et al.²². This phenomenon is attributed to the trapping phenomenon discussed in Point defect transport mechanism near dislocation loop. Since the kinetic energy of the system increases with temperature, it is easier for SIAs to overcome the MEBs, reducing the time a SIA remains in the trapping region (i.e., reducing the lifetime τ_i). In contrast, there is no trapping region for vacancies.

The obtained dislocation loop bias is substantially lower than that of straight dislocations calculated by previous studies^{10,22,26–29,57,58}, as shown in Fig. 4, even screw dislocation bias calculated using the same approach²⁹. Note that the bias value of a screw dislocation from Bakaev et al.²⁸ is close to the loop bias in this study. However, this may be a coincidence since Chang et al.²⁶ and Bakaev et al.²⁸ also reported negative bias for screw dislocations under other conditions. For example, these studies have reported bias values between -0.04 and -0.06 in the atomistic-analytical screw dislocation case without external stress, which may indicate systematic underestimation. Bias factors of loops in this study are also significantly lower than those of edge dislocations, either compared with calculations based on the drift-diffusion model and the elasticity theory by Wolfer¹⁰, Seif et al.²²,

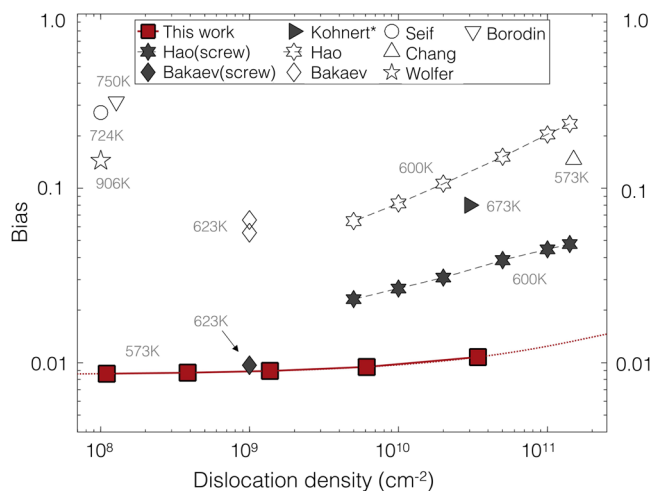


Fig. 4 A comparison of loop bias in this study and straight dislocation bias from previous theoretical calculations. Data points close to 573 K are selected. The bias factors of screw dislocations are labeled by filled markers and edge dislocations by hollow markers. The (*) mark indicates a mixture of both dislocations, whereas screw dislocations are dominant (80% screw – 20% edge).

and Borodin et al.⁵⁷, or those calculated using atomistic approaches provided by Bakaev et al.²⁸, Chang et al.²⁶, and Kohnert et al.⁵⁸.

Comparisons with experimental results. The estimated swelling rates are compared with experimental results^{31–38,59,60}, shown in Fig. 5, which accounts for the sink strength of dislocation loops, straight dislocations (screw dislocations, data from Hao et al.²⁹), and voids. The density of loops, dislocations, and voids, as well as the void sizes in the calculation, are based on the experimental results of Horton’s work³¹ since it provides very detailed data of microstructures.

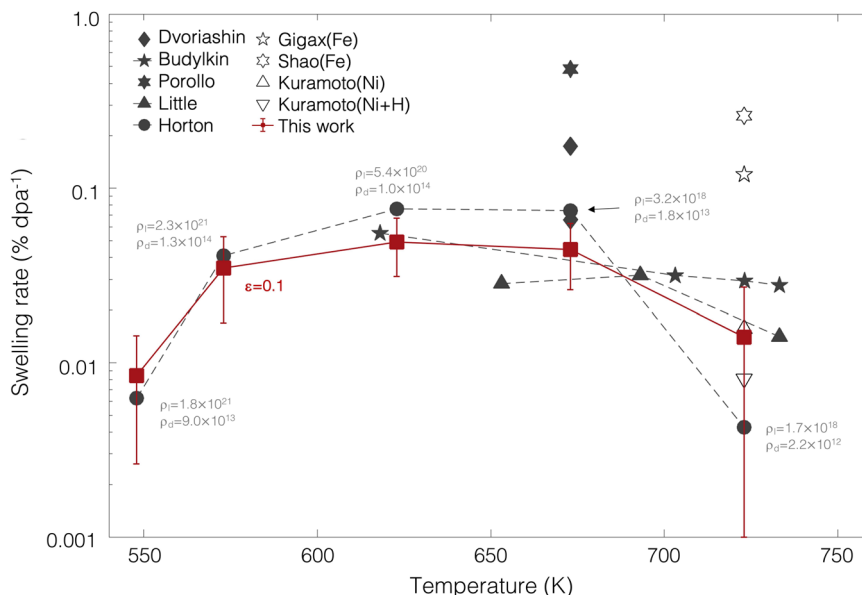


Fig. 5 A comparison of swelling rates in bcc iron between this work and experimental results. Filled and hollow symbols stand for neutron and ion irradiations, respectively. ρ_l stands for loop density (m^{-3}), ρ_d for dislocation density (m^{-2}). Microstructure information comes from Horton et al.³¹.

Both the calculations of this study and experimental results show that the void swelling rate increases with increasing temperature until reaching a peak value (at ~ 673 K) and declines with higher temperatures after the peak^{31,32}. Before reaching the temperature where peak swelling occurs, small loops (5 nm–21.5 nm in radii) have been observed in ref.³¹ as the dominant microstructure feature with high densities ($> 10^{20} \text{ m}^{-3}$), indicating that dislocation loops play a critical role in void swelling within this temperature range. The calculated swelling rates increase from 0.008 % dpa⁻¹ to 0.049 % dpa⁻¹, which is consistent with experimental data from Horton et al.³¹ and Budylnkin et al.³³, corroborating the increasing loop bias. Alternatively, the contribution of straight dislocations to the void swelling changes little in this temperature range since the dislocation density ($\sim 10^{14} \text{ m}^{-2}$) and structure change little before reaching the temperature where peak swelling occurs³¹.

At 673 K, the calculated swelling rate from this study is ~ 0.044 % dpa⁻¹, which is consistent with the average value of several experimental studies^{31–35}, although the residual impurities³², irradiation dose rates³³, and cold-work level of samples^{34,35} may cause fluctuation of results in individual experimental studies. When the temperature exceeds ~ 700 K, the vacancy emission dominates the void swelling, significantly limiting the void growth in experiments⁶¹. Based on our calculations (details in Supplementary Note 6), voids will lose 75.1% of their volumes at 723 K, because of which the bias of sinks is no longer the leading factor for the overall swelling rate, although loop bias factors increase with increasing temperature. The calculated temperature dependence over 673 K is also consistent with experimental results^{31–33,36}, which is a significant improvement compared with previous theoretical studies.

Conclusions

The loop core effects and the cumulative effects of millions of MEBs significantly influence the defect transport properties of point defects. Based on the obtained MEBs and diffusion tendency, a mechanistic understanding of point defect diffusion near a dislocation loop in α -iron is developed. We identify two diffusion paths of a SIA near the dislocation loop, depending on the initial position of the defect. For Path I, a mobile SIA near the habit plane of the loop tends to be absorbed directly by the edge

of the loop. For Path II, a SIA away from the habit plane of the loop diffuses along curved pathways toward the habit plane region. This mechanism results in trapping regions near the loop, which prolongs the lifetime of a SIA and leads to lower capture efficiency, which subsequently impacts the sink strengths and bias values of dislocation loops.

The $< 100 >$ interstitial loop bias factors are lower than 0.1 with radii between 2 nm and 5 nm, substantially lower than those of straight dislocations. This conclusively demonstrates the significance of including atomistic details of the interaction between point defects and loops to void swelling. The calculated swelling rates increase with rising temperatures before peak swelling and decrease after 673 K due to the domination of vacancy emission from voids. These results confirm we have considered the decisive aspects of void swelling in irradiated α -iron across varying temperatures.

Finally, the exceptional agreement with experimental results constitutes extraordinary progress in swelling performance prediction and microstructural evolution simulation in irradiated materials. The generality of this approach allows straightforward extensions to provide insights into a variety of other situations as well, for example, modeling the interaction of microstructures and point defects in other structural materials, such as fcc metals or alloys.

Methodology

The lifetime, capture efficiency, and bias factor of point defects.

The lifetime of a defect is defined as the time required for the point defect to diffuse from an initial position to a sink, which can be a dislocation loop, a straight dislocation, a void, etc. With the lifetime of a point defect, the capture efficiency can be defined following the approach derived in Hao et al.²⁹,

$$Z_{\alpha} = \frac{\tau_{\alpha}^r}{\tau_{\alpha}}$$

where τ_{α} represents the lifetime of the point defect α , e.g., a SIA or a vacancy, under the influence of a sink, denoted as real walk in this paper. In comparison, the superscript r refers to random walk diffusion, which is the lifetime of a point defect without the interaction with the sink. The capture efficiency is the ratio of τ_{α}^r and τ_{α} , which quantifies the preferential diffusion of a point

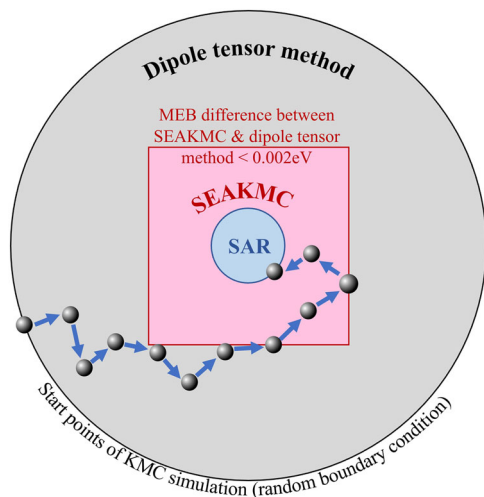


Fig. 6 The schematics of the AKMC simulation setup. The dipole tensor method is employed in the grey region, and the SEAKMC is employed in the pink region. SAR is shown as the blue circle in the center. Black spheres show an example of the point defect diffusion trajectory.

defect to a specific sink with reference to bulk diffusion. The lifetime of the point defect is found to be proportional to the volume of simulation system, as demonstrated in Supplementary Fig. 5. This relationship can be utilized to predict the point defect lifetime in larger systems. The tendency of efficient absorption by the sink corresponds to a higher value of Z_α . Following Golubov et al.⁵⁶, the bias factor B of a specific sink is determined from the capture efficiencies of SIAs and vacancies using the following equation

$$B = \frac{Z_i - Z_v}{Z_v}$$

in which the subscripts i and v stand for SIA and vacancy, respectively. The bias factor quantifies the preferential absorption of SIAs compared with vacancies for a specific sink. Therefore, the bias factor can be calculated by substituting capture efficiencies with lifetimes:

$$B = \frac{\frac{\tau_i^r}{\tau_i} - \frac{\tau_v^r}{\tau_v}}{\frac{\tau_v^r}{\tau_v}} = \frac{\tau_i^r \tau_v}{\tau_v^r \tau_i} - 1$$

Swelling rate calculation. Swelling rate calculation is derived in refs. 21,56 and calculated based on the sink strength for comparison with experimental results

$$\text{Swelling rate} = \varepsilon * k_v^2 * \frac{k_{l,i}^2 + k_{d,i}^2 - k_{l,v}^2 - k_{d,v}^2}{(k_V^2 + k_{l,v}^2 + k_{d,v}^2)(k_V^2 + k_{l,i}^2 + k_{d,i}^2)} * (1 - J_v^{\text{em}}/N)$$

where ε is the survival fraction of point defects, which means the fraction of the Frenkel pairs escaping the in-cascade recombination, dependent on materials and irradiation conditions, usually between 0.1 and 0.3^{62–64}. This term provides the number of mobile point defects that should be considered in the diffusion calculations. The survival fraction ε is selected to be 0.1 in this study based on earlier atomistic simulations of displacement cascades and subsequent annealing in bcc iron^{64,65}. k^2 represents the sink strength in the ideal system, subscript V stands for the void, l for the dislocation loop, and d for the straight dislocation. J_v^{em} is the vacancy emission rate^{56,66}, and N is the number of vacancies contained in a void.

Migration energy barrier (MEB) calculation. Point defect migration to the first nearest neighbors is considered for MEB

calculations, with bulk values equal to 0.3075 eV and 0.6401 eV for an SIA and a vacancy, respectively, based on the potential developed by Ackland et al.⁶⁷. MEBs close to the loop core (about 58.54 million saddle points in a $23 * 23 * 23 \text{ nm}^3$ simulation box for a 5 nm loop) are calculated using SEAKMC^{52,64}. The MEBs far from the loop core are calculated using the dipole tensor method^{68,69}. As designed, the differences between MEBs on the edge of the box calculated using SEAKMC and the dipole tensor method are less than 0.002 eV. Detailed information is provided in Supplementary Note 1.

Atomistic kinetic Monte Carlo (AKMC). AKMC is employed to calculate the lifetime of a point defect. The setup of AKMC is shown in Fig. 6. A spherical system is set with the dislocation loop located at the center of the sphere, which is equivalent to uniform distribution of loops. The SAR is defined in this work as the region where the sink spontaneously absorbs the point defect. Areas in red and grey are the regions in which the MEBs are calculated by SEAKMC and the dipole tensor method, respectively. Random boundary conditions²⁹ are employed to reduce the anisotropic impacts at low temperatures and high dislocation loop density simulations. Following this setup, the lifetime of a point defect is the statistical average diffusion time starting from the boundary to the SAR. The statistical accuracy is provided in Supplementary Fig. 6.

Loop construction and spontaneous absorption region (SAR) using LAMMPS. In bcc iron, $\langle 100 \rangle$ interstitial loops are the dominant type of dislocation loop in irradiated iron^{31,70}. The configuration of a $[100]$ interstitial loop is constructed by inserting two layers of SIAs into a perfect bcc system with the Burger's vector along the z-axis ($[001]$), while the x-axis is $[100]$, and the y-axis is $[010]$. The interatomic potential developed by Ackland et al.⁶⁷ is employed for structural relaxation using LAMMPS⁵⁰. SARs have been determined based on the binding energies of point defects using the same potential. The criteria are set to be lower than -0.1 eV and -0.05 eV for an SIA and a vacancy, respectively. The definition of binding energy is the same as the interaction energy in Chang et al.²⁶, which is the difference in the formation energy with and without the loop:

$$E^{\text{Binding}} = E_{\text{with loop}}^{\text{Formation}} - E_{\text{in bulk}}^{\text{Formation}}$$

The SAR for random walks of SIAs and vacancies is the same in this work as the reference state for real walks.

Data availability

All raw data included in this work are openly available at figshare repository <https://figshare.com/s/ebf6dad08914eb277d87>. All other relevant data are available from the corresponding author upon reasonable request.

Received: 5 December 2022; Accepted: 18 April 2023;
Published online: 06 May 2023

References

1. Arakawa, K. et al. Observation of the one-dimensional diffusion of nanometer-sized dislocation loops. *Science* **318**, 956–959 (2007).
2. Arakawa, K., Hatanaka, M., Kuramoto, E., Ono, K. & Mori, H. Changes in the burgers vector of perfect dislocation loops without contact with the external dislocations. *Phys. Rev. Lett.* **96**, 125506 (2006).
3. Bai, X. M., Voter, A. F., Hoagland, R. G., Nastasi, M. & Uberuaga, B. P. Efficient annealing of radiation damage near grain boundaries via interstitial emission. *Science* **327**, 1631–1634 (2010).
4. Beyerlein, I. J., Demkowicz, M. J., Misra, A. & Uberuaga, B. P. Defect-interface interactions. *Prog. Mater. Sci.* **74**, 125–210 (2015).

5. Cawthorne, C. & Fulton, E. J. Voids in irradiated stainless steel. *Nature* **216**, 575–576 (1967).
6. Greenwood, G. W., Foreman, A. J. E. & Rimmer, D. E. The role of vacancies and dislocations in the nucleation and growth of gas bubbles in irradiated Fissile material. *J. Nucl. Mater.* **1**, 305–324 (1959).
7. Garner, F. A. Recent insights on the swelling and creep of irradiated austenitic alloys. *J. Nucl. Mater.* **122**, 459–471 (1984).
8. Garner, F. A., Toloczko, M. B. & Sencer, B. H. Comparison of swelling and irradiation creep behavior of fcc-austenitic and bcc-ferritic/martensitic alloys at high neutron exposure. *J. Nucl. Mater.* **276**, 123–142 (2000).
9. Heald, P. T. Preferential trapping of interstitials at dislocations. *Philos. Mag.* **31**, 551–558 (1975).
10. Wolfer, W. G. The dislocation bias. *J. Comput.-Aided Mater.* **14**, 403–417 (2007).
11. Xu, W. Z. et al. In-situ atomic-scale observation of irradiation-induced void formation. *Nat. Commun.* **4**, 2288 (2013).
12. Mansur, L. K. Void Swelling in metals and alloys under irradiation - Assessment of theory. *Nucl. Technol.* **40**, 5–34 (1978).
13. Zinkle, S. J. & Was, G. S. Materials challenges in nuclear energy. *Acta. Mater.* **61**, 735–758 (2013).
14. Bullough, R., Eyre, B. L. & Krishan, K. Cascade damage effects on swelling of irradiated materials. *Proc. Royal Soc. London Series a-Mathematical Phys. Eng. Sci.* **346**, 81–102 (1975).
15. Brailsford, A. D. & Bullough, R. Rate theory of swelling due to void growth in irradiated metals. *J. Nucl. Mater.* **44**, 121–12 (1972).
16. Bulatov, V., Abraham, F. F., Kubin, L., Devincere, B. & Yip, S. Connecting atomistic and mesoscale simulations of crystal plasticity. *Nature* **391**, 669–672 (1998).
17. Bulatov, V. & Cai, W. *Computer simulations of dislocations*. Vol. 3 (OUP Oxford, 2006).
18. Li, J., Van Vliet, K. J., Zhu, T., Yip, S. & Suresh, S. Atomistic mechanisms governing elastic limit and incipient plasticity in crystals. *Nature* **418**, 307–310 (2002).
19. Osetsky, Y. N. & Bacon, D. J. An atomic-level model for studying the dynamics of edge dislocations in metals. *Model Simul. Mater. Sc.* **11**, 427–446 (2003).
20. Yamakov, V., Wolf, D., Phillpot, S. R., Mukherjee, A. K. & Gleiter, H. Deformation-mechanism map for nanocrystalline metals by molecular-dynamics simulation. *Nat. Mater.* **3**, 43–47 (2004).
21. Mansur, L. K. Theory and experimental background on dimensional changes in irradiated alloys. *J. Nucl. Mater.* **216**, 97–123 (1994).
22. Seif, D. & Ghoniem, N. M. Effect of anisotropy, SIA orientation, and one-dimensional migration mechanisms on dislocation bias calculations in metals. *J. Nucl. Mater.* **442**, S633–S638 (2013).
23. Woo, C. H. & Singh, B. N. Production Bias due to clustering of point-defects in irradiation-induced cascades. *Philos. Mag. A* **65**, 889–912 (1992).
24. Woo, C. H. & Singh, B. N. The concept of production bias and its possible role in defect accumulation under cascade damage conditions. *Phys. Status Solidi B* **159**, 609–616 (1990).
25. Carpentier, D., Jourdan, T., Le Bouar, Y. & Marinica, M. C. Effect of saddle point anisotropy of point defects on their absorption by dislocations and cavities. *Acta. Mater.* **136**, 323–334 (2017).
26. Chang, Z. W., Terentyev, D., Sandberg, N., Samuelsson, K. & Olsson, P. Anomalous bias factors of dislocations in bcc iron. *J. Nucl. Mater.* **461**, 221–229 (2015).
27. Chang, Z., Olsson, P., Terentyev, D. & Sandberg, N. Multiscale calculations of dislocation bias in fcc Ni and bcc Fe model lattices. *Nucl. Instrum. Meth. B* **352**, 81–85 (2015).
28. Bakaev, A. et al. Effect of isotropic stress on dislocation bias factor in bcc iron: an atomistic study. *Philos. Mag.* **98**, 54–74 (2018).
29. Hao, J. N., Luis, C.-T., Xu, H. X. Using lifetime of point defects for dislocation bias in bcc Fe. *Curr. Opin. Solid State Mater. Sci.* **26**, 101021 (2022).
30. Xu, H. X., Stoller, R. E., Osetsky, Y. N. & Terentyev, D. Solving the Puzzle of <100> Interstitial Loop Formation in bcc Iron. *Phys. Rev. Lett.* **110**, 265503 (2013).
31. Horton, L. L., Bentley, J. & Farrell, K. A Tem study of neutron-irradiated iron. *J. Nucl. Mater.* **108**, 222–233 (1982).
32. Little, E. A. & Stow, D. A. Voids-swelling in irons and ferritic steels .2. Experimental survey of materials irradiated in a fast-reactor. *J. Nucl. Mater.* **87**, 25–39 (1979).
33. Budylnin, N. I. et al. Neutron-induced swelling and embrittlement of pure iron and pure nickel irradiated in the BN-350 and BOR-60 fast reactors. *J. Nucl. Mater.* **375**, 359–364 (2008).
34. Porollo, S. I., Dvoriashin, A. M., Vorobyev, A. N. & Konobeev, Y. V. The microstructure and tensile properties of Fe-Cr alloys after neutron irradiation at 400 degrees C to 5.5-7.1 dpa. *J. Nucl. Mater.* **256**, 247–253 (1998).
35. Dvoriashin, A. M., Porollo, S. I., Konobeev, Y. V. & Garner, F. A. Influence of cold work to increase swelling of pure iron irradiated in the BR-10 reactor to similar to 6 and similar to 25 dpa at similar to 400 degrees C. *J. Nucl. Mater.* **283**, 157–160 (2000).
36. Kuramoto, E. et al. Simulation irradiation studies on iron. *J. Nucl. Mater.* **103**, 1091–1095 (1982).
37. Brimbal, D., Meslin, E., Henry, J., Decamps, B. & Barbu, A. He and Cr effects on radiation damage formation in ion-irradiated pure iron and Fe-5.40 wt.% Cr: A transmission electron microscopy study. *Acta. Mater.* **61**, 4757–4764 (2013).
38. Bhattacharya, A. et al. Effect of chromium on void swelling in ion irradiated high purity Fe-Cr alloys. *Acta. Mater.* **108**, 241–251 (2016).
39. Woo, C. H. The sink strength of a dislocation loop in the effective medium approximation. *J. Nucl. Mater.* **98**, 279–294 (1981).
40. Rouchette, H., Thuinet, L., Legris, A., Ambard, A. & Domain, C. Numerical evaluation of dislocation loop sink strengths: A phase-field approach. *Nucl. Instrum. Meth. B* **352**, 31–35 (2015).
41. Bullough, R., Hayns, M. R. & Woo, C. H. Sink strength of dislocation loops and their growth in irradiated materials. *J. Nucl. Mater.* **84**, 93–100 (1979).
42. Khraishi, T. A., Hirth, J. P., Zbib, H. M. & de La Rubia, T.D. The stress field of a general circular Volterra dislocation loop: analytical and numerical approaches. *Phil. Mag. Lett.* **80**, 95–105 (2000).
43. Khraishi, T. A., Hirth, J. P., Zbib, H. M. & Khaleel, M. A. The displacement, and strain-stress fields of a general circular Volterra dislocation loop. *Int. J. Eng. Sci.* **38**, 251–266 (2000).
44. Brailsford, A. D., Bullough, R. & Hayns, M. R. Point-defect sink strengths and void-swelling. *J. Nucl. Mater.* **60**, 246–256 (1976).
45. Dubinko, V. I., Abyzov, A. S. & Turkin, A. A. Numerical evaluation of the dislocation loop bias. *J. Nucl. Mater.* **336**, 11–21 (2005).
46. Thuinet, L., Rouchette, H. & Legris, A. 3D phase-field modelling of dislocation loop sink strengths. *J. Nucl. Mater.* **483**, 62–81 (2017).
47. Rouchette, H., Thuinet, L., Legris, A., Ambard, A. & Domain, C. Quantitative phase field model for dislocation sink strength calculations. *Comp. Mater. Sci.* **88**, 50–60 (2014).
48. Masters, B. C. Dislocation loops in irradiated iron. *Philos. Mag.* **11**, 881–88 (1965).
49. Little, E. A., Bullough, R. & Wood, M. H. On the swelling resistance of ferritic steel. *P. Roy. Soc. Lond. a Mat.* **372**, 565–56 (1980).
50. Plimpton, S. Fast parallel algorithms for short-range molecular-dynamics. *J. Comput. Phys.* **117**, 1–19 (1995).
51. Xu, H. X., Osetsky, Y. N. & Stoller, R. E. Self-evolving atomistic kinetic Monte Carlo: fundamentals and applications. *J. Phys-Condens. Mat.* **24**, 375402 (2012).
52. Xu, H. X., Stoller, R. E., Beland, L. K. & Osetsky, Y. N. Self-evolving atomistic kinetic Monte Carlo simulations of defects in materials. *Comput. Mater. Sci.* **100**, 135–143 (2015).
53. Chai, J., Jin, S., Yu, Z., Xu, H. X. & Lu, G. H. Capture efficiency and bias from the defect dynamics near grain boundaries in BCC Fe using mesoscale simulations. *J. Mater. Sci. Technol.* **93**, 169–177 (2021).
54. McElfresh, C., Bertin, N., Aubry, S. & Marian, J. Coalescence dynamics of prismatic dislocation loops due to vacancy supersaturation. *Phys. Rev. Mater.* **6** (2022). ARTN L100601 <https://doi.org/10.1103/PhysRevMaterials.6.L100601>.
55. McElfresh, C., Bertin, N., Aubry, S. & Marian, J. A parallel discrete dislocation dynamics/kinetic Monte Carlo method to study non-conservative plastic processes. *Comput. Mater. Sci.* **209** (2022). ARTN 111332 <https://doi.org/10.1016/j.commatsci.2022.111332>.
56. Golubov, S. I., Barashev, A. V. & Stoller, R. E. Radiation Damage Theory. *Comprehensive Nuclear Materials, Vol 1: Basic Aspects of Radiation Effects in Solids/Basic Aspects of Multi-Scale Modeling*, 357–391 (2012).
57. Borodin, V. A. & Ryazanov, A. I. The effect of diffusion anisotropy on dislocation bias and irradiation creep in cubic lattice materials. *J. Nucl. Mater.* **210**, 258–267 (1994).
58. Kohnert, A. A. & Capolungo, L. Sink strength and dislocation bias of three-dimensional microstructures. *Phys. Rev. Mater.* **3** (2019).
59. Gigax, J. G. et al. The influence of ion beam rastering on the swelling of self-ion irradiated pure iron at 450 degrees C. *J. Nucl. Mater.* **465**, 343–348 (2015).
60. Shao, L. et al. Effect of defect imbalance on void swelling distributions produced in pure iron irradiated with 3.5 MeV self-ions. *J. Nucl. Mater.* **453**, 176–181 (2014).
61. Was, G. S. *Fundamentals of radiation materials science: metals and alloys*. (Springer, 2007).
62. Averback, R. S., Benedek, R. & Merkle, K. L. Ion-Irradiation Studies of the Damage Function of Copper and Silver. *Phys. Rev. B* **18**, 4156–4171 (1978).
63. Stoller, R. E. Point defect survival and clustering fractions obtained from molecular dynamics simulations of high energy cascades. *J. Nucl. Mater.* **233**, 999–1003 (1996).
64. Xu, H. X., Osetsky, Y. N. & Stoller, R. E. Cascade annealing simulations of bcc iron using object kinetic Monte Carlo. *J. Nucl. Mater.* **423**, 102–109 (2012).
65. Zinkle, S. J. & Stoller, R. E. Quantifying defect production in solids at finite temperatures: Thermally-activated correlated defect recombination

- corrections to DPA (CRC-DPA). *J. Nucl. Mater.* **577** <https://doi.org/10.1016/j.jnucmat.2023.154292> (2023).
66. Barashev, A. V., Golubov, S. I., Osetsky, Y. N. & Stoller, R. E. Dissociation of migrating particle from trap with long-range interaction field. *Philosophical Magazine* **90**, 907–921 (2010).
67. Ackland, G. J., Mendeleev, M. I., Srolovitz, D. J., Han, S. & Barashev, A. V. Development of an interatomic potential for phosphorus impurities in alpha-iron. *J. Phys.-Condens. Mat.* **16**, S2629–S2642 <https://doi.org/10.1088/0953-8984/16/27/003> (2004).
68. Clouet, E., Varvenne, C. & Jourdan, T. Elastic modeling of point-defects and their interaction. *Comp. Mater. Sci.* **147**, 49–63 (2018).
69. Varvenne, C. & Clouet, E. Elastic dipoles of point defects from atomistic simulations. *Phys. Rev. B.* **96**, 224103 (2017).
70. Yao, Z., Hernandez-Mayoral, M., Jenkins, M. L. & Kirk, M. A. Heavy-ion irradiations of Fe and Fe-Cr model alloys Part 1: Damage evolution in thin-foils at lower doses. *Philos. Mag.* **88**, 2851–2880 (2008).
71. Stukowski, A. Visualization and analysis of atomistic simulation data with OVITO-the Open Visualization Tool. *Model. Simul. Mater. Sc.* **18** (2010). Artn 015012. <https://doi.org/10.1088/0965-0393/18/1/015012>

Acknowledgements

This work is supported by the US Department of Energy, Office of Science, Basic Energy Sciences, under Award No. DE-SC0019151. This research used resources of the National Energy Research Scientific Computing Center, a DOE Office of Science User Facility supported by the Office of Science of the US Department of Energy under Contract No. DE-AC02-05CH11231.

Author contributions

Z.Y.: Investigation, Methodology, Validation, Formal analysis, Writing – original draft, Visualization. H.X.: Conceptualization, Methodology, Formal analysis, Writing – review & editing, Supervision, Project administration, Funding acquisition.

Competing interests

The authors declare no competing interests.

Additional information

Supplementary information The online version contains supplementary material available at <https://doi.org/10.1038/s43246-023-00356-5>.

Correspondence and requests for materials should be addressed to Haixuan Xu.

Peer review information *Communications Materials* thanks the anonymous reviewers for their contribution to the peer review of this work. Primary Handling Editors: Jet-Sing Lee and John Plummer.

Reprints and permission information is available at <http://www.nature.com/reprints>

Publisher's note Springer Nature remains neutral with regard to jurisdictional claims in published maps and institutional affiliations.



Open Access This article is licensed under a Creative Commons Attribution 4.0 International License, which permits use, sharing, adaptation, distribution and reproduction in any medium or format, as long as you give appropriate credit to the original author(s) and the source, provide a link to the Creative Commons license, and indicate if changes were made. The images or other third party material in this article are included in the article's Creative Commons license, unless indicated otherwise in a credit line to the material. If material is not included in the article's Creative Commons license and your intended use is not permitted by statutory regulation or exceeds the permitted use, you will need to obtain permission directly from the copyright holder. To view a copy of this license, visit <http://creativecommons.org/licenses/by/4.0/>.

© The Author(s) 2023